



PAPER

[View Article Online](#)
[View Journal](#) | [View Issue](#)Cite this: *Green Chem.*, 2024, **26**,
1443

Tailoring metal–support interaction over faceted TiO₂ and copper nanoparticles for electrocatalytic nitrate reduction to ammonia†

Wahyu Prasetyo Utomo,^a Hao Wu,^{*b} Rui Liu ^a and Yun Hau Ng ^{*a}

The electrocatalytic nitrate reduction reaction (NO₃[−]RR) provides a sustainable route for ammonia production while mitigating nitrate pollutants in the environment. Metal–support interaction has a significant influence on this electrocatalytic process. However, the mechanism of the facet-dependent metal–support interaction in the NO₃[−]RR is still unknown. Herein, we report the modulation of the metal–support interaction by depositing copper nanoparticles on anatase TiO₂ with different facet exposures, *i.e.*, (001) and (101) facets. The result of copper nanoparticles being deposited on TiO₂ with dominant (101) facet exposure is an enhanced ammonia yield rate of 447.5 μg mg_{cat}^{−1} h^{−1} at −0.9 V vs. reversible hydrogen electrode (RHE), which is 4.2 times higher than the pristine TiO₂ counterpart. The strong interaction between copper nanoparticles and TiO₂ with dominant (101) facet exposure contributes to a greater increase in catalytic performance than TiO₂ with dominant (001) facet exposure. The strong interaction leads to electron-deficient copper nanoparticles, efficient electron transfer, and stronger binding of the *NO₂ intermediate, promoting the hydrogenation process in the NO₃[−] reduction reaction for selective NH₃ synthesis.

Received 8th June 2023,
Accepted 4th December 2023

DOI: 10.1039/d3gc02018e

rsc.li/greenchem

Introduction

Ammonia (NH₃) is an essential feedstock chemical for the fertilizer, pharmaceutical, and nitrogen-containing chemical industries, as well as a potential energy carrier.^{1–5} Nevertheless, the production of NH₃ still heavily relies on the Haber–Bosch process, which requires high temperature (400–500 °C) and high pressure (100–200 atm).^{6,7} Annually, this process needs an energy supply of up to ~2.5 exajoule and is responsible for 1.4% of carbon dioxide emissions.^{8,9} Therefore, the development of a more energy-saving and environmentally friendly process is important.

The electrocatalytic nitrate reduction reaction (NO₃[−]RR) to NH₃ has attracted increasing attention as an alternative method for sustainable NH₃ production since it can be performed under ambient conditions. Moreover, NO₃[−] is highly soluble in water and is known as one of the most widespread

pollutants in the environment, especially in water bodies. NO₃[−] mainly comes from industrial wastewater, liquid nuclear waste, livestock excrement, and chemical fertilizers, with a wide range of concentrations up to 2 mol L^{−1}.^{10,11} The increased concentration of NO₃[−] could lead to eutrophication, which decreases the oxygen level in water and destroys aquatic ecosystems.^{12–16} From a thermodynamic point of view, NO₃[−] has a lower dissociation energy of the N=O bond (204 kJ mol^{−1}), which could be more readily reduced with a lower thermodynamic barrier compared to bonds in other nitrogen-containing sources, such as N₂.¹⁷ Therefore, the process of converting NO₃[−] to NH₃ *via* the NO₃[−]RR could potentially provide a sustainable route for green NH₃ synthesis and address current issues with environmental water pollution.

Several electrocatalysts have been developed for the NO₃[−]RR, such as titanium dioxide (TiO₂), copper(II) oxide (CuO), copper(I) oxide (Cu₂O), and cobalt oxide (CoO).^{18–21} However, the exhibited performance is typically still limited and remains far below the practical performances as mentioned by the US Department of Energy (300 mA cm^{−2} with 90% faradaic efficiency for NH₃, FE_{NH₃}).²² Continuous studies and investigations are still needed to acquire a better understanding of the catalytic system; hence, the catalytic performance can be further improved. In this regard, exposing specific facets of the catalyst is a promising strategy to modulate catalytic activity as different facet exposures reveal different atomic

^aLow-Carbon and Climate Impact Research Centre, School of Energy and Environment, City University of Hong Kong, Kowloon, Hong Kong SAR 999077, China. E-mail: yunhau.ng@cityu.edu.hk

^bMacao Institute of Materials Science and Engineering (MIMSE), Faculty of Innovation Engineering, Macau University of Science and Technology, Taipa, Macau SAR 999078, China. E-mail: wuhao@must.edu.mo

†Electronic supplementary information (ESI) available: Experimental procedure, Fig. S1–S19 and Tables S1 and S2. See DOI: <https://doi.org/10.1039/d3gc02018e>

arrangements and electronic properties.^{23–28} Typically, the (001) facet of anatase TiO₂ was reported to have higher reactivity due to the dominance of undercoordinated Ti atoms. An ideal (001) surface of TiO₂ is occupied by five-coordinated Ti (Ti_{5c}), *i.e.*, undercoordinated Ti, accounting for 100% of coverage. On the other hand, the (101) surface is occupied by 50% Ti_{5c} and 50% six-coordinated Ti (Ti_{6c}).^{29–31} Therefore, the exposure of more (001) facets can, theoretically, lead to higher activity due to the more reactive Ti_{5c} species on the surface. Other factors, such as electronic properties, band energy, or electron trapping states, can also contribute to the different catalytic performances induced by the facet effect.^{29,32–36} As reported by Pan *et al.*, TiO₂ with (010) facet exposure (TiO₂-010) showed the highest catalytic activity, followed by TiO₂-101 and TiO₂-001.²⁹ The performances exhibited were attributed to the cooperative effects of the undercoordinated Ti (Ti_{5c}) on the (010) surface of TiO₂-(010), and a more energetic conduction band (CB) position resulting in stronger reducing electrons in the CB. Besides, Mikrut *et al.* reported that the TiO₂-(100) catalyst showed the highest activity toward the catalytic oxidation reaction compared to its TiO₂-(001) and the TiO₂-(101) counterparts.³² The superior performance was contributed to by the promoted separation of charge carriers in the TiO₂-(100) catalyst, which facilitated hole transfer to the active sites. Moreover, Sun *et al.* reported a silver (Ag)-loaded TiO₂ for a catalytic NO₃[–]RR.³³ Benefitting from the Ag nanoparticles as trap centres for electron transfer, the removal efficiency of NO₃[–] reached ~95% with high selectivity of 90% towards N₂ production.

In addition to facet control, metal loading is another effective way to improve the catalytic activity of the NO₃[–]RR. For instance, Kim *et al.* reported the strong metal-support interaction between the Pd–Cu cocatalyst and oxygen-deficient TiO₂, promoting interfacial electron transfer and enhancing the NO₃[–]RR performance.³⁷ Nevertheless, NO₂[–] is still the dominant product instead of the desired NH₃ using the reported catalysts. Following this study, Li *et al.* reported using Pd–In supported on an FeO_x substrate as the catalyst.³⁸ The intrinsic electron transfer from Pd to the support led to the formation of positively charged Pd sites, which facilitates the adsorption of NO₃[–] for better activation. A similar result was also observed in Cu–Pd-loaded nitrogen-doped carbon (Cu–Pd/CN). The interaction between Cu–Pd nanoparticles and the CN support stimulated the interfacial charge polarization and resulted in the electron-deficient Cu as the active site, which is favourable for NO₃[–] adsorption and activation.³⁹

The aforementioned studies indicate the significance of facet exposure and metal-support interaction on the catalytic performance for the NO₃[–]RR. However, the determining factor in the electrocatalytic activity for the faceted TiO₂ is still debatable since many factors could contribute to the apparent catalytic activity.^{29,30,33,34} Moreover, the contribution of the exposed TiO₂ facet to the metal-support interaction in metal-loaded faceted TiO₂ in correlation with their electrocatalytic performance for the NO₃[–]RR remains unclear. The deposition of metal on the specific facet of TiO₂ can lead to different

levels of metal-support interaction due to the differing natures of the specific facets of TiO₂. It can also lead to different reactivities during the catalytic process. In this context, Cu nanoparticles are deposited on the surface of TiO₂ with different facet exposures, *i.e.*, (001) and (101) facets, and catalytic tests toward the NO₃[–]RR as a proof of concept of tailoring the interaction between metal and support are performed. The strong metal-support interaction between the Cu nanoparticles and (101) facets lead to effective electron transfer from the Cu nanoparticles to the TiO₂ support resulting in electron-deficient Cu. In addition to the oxygen vacancies (OVs) in the TiO₂ support, the electron-deficient Cu nanoparticles then serve as active sites for the NO₃[–] adsorption and may also supply the NO₃[–] reactants to the nearby OVs of TiO₂. As a result, the production of NH₃ by the (101)-dominant Cu-TiO₂ electrocatalyst reaches the highest yield rate of 447.5 μg mg_{cat}^{–1} h^{–1} at –0.9 V *vs.* reversible hydrogen electrode (RHE) among its prepared counterparts, which is 4.2 times higher than that of the pristine (101)-dominant TiO₂ (NH₃ yield: 106.7 μg mg_{cat}^{–1} h^{–1}). The increase is more exaggerated compared to the enhancement exhibited by the (001)-dominant Cu-TiO₂ with respect to the pristine (001)-dominant TiO₂. Moreover, time-dependent experiments and electrochemical analysis disclose that strong metal-support interaction results in a more strongly binding *NO₂ intermediate, which promotes the electron transfer, facilitating the subsequent hydrogenation process for the selective NH₃ synthesis.

Results and discussion

Material characterization

The TiO₂ catalyst with (001) facet or (101) facet as the dominant facet is denoted as (001)-dominant TiO₂ and (101)-dominant TiO₂, respectively, which was prepared by a hydrothermal process using NaF as a capping agent (details in the Experimental section).^{32,40} Subsequently, Cu nanoparticles were evenly deposited on the surface of (001)-dominant TiO₂ and (101)-dominant TiO₂, resulting in (001)-dominant Cu-TiO₂ and (101)-dominant Cu-TiO₂ (details in the Experimental section). X-ray diffraction (XRD) patterns of the prepared catalysts are presented in Fig. 1a. All XRD peaks can be indexed to the anatase TiO₂ (JCPDS 98-105-4604) without the rutile phase being observed.^{31,41} The peak intensities of the (001)-dominant Cu-TiO₂ and (101)-dominant Cu-TiO₂ are slightly lower than those of the pristine (001)-dominant TiO₂ and (101)-dominant TiO₂, which indicate slight decreases in crystallinity. The decline in the crystallinity can be correlated with the slight reduction of pristine TiO₂ by NaBH₄ during the Cu deposition process.⁴² However, no additional peaks from the deposited Cu can be observed in the XRD patterns because of the low amount of deposited Cu and its high dispersion.⁴³ Inductively coupled plasma optical emission spectroscopy (ICP-OES) analysis shows that the amounts of loaded Cu are 0.86% w/w and 0.82% w/w for the (001)-dominant Cu-TiO₂ and (101)-dominant Cu-TiO₂, respectively.

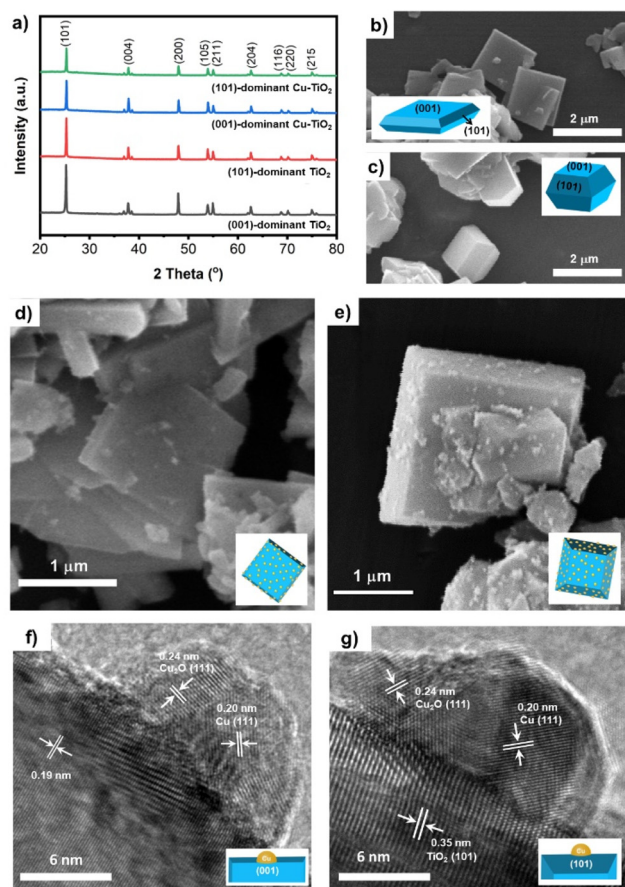


Fig. 1 (a) XRD patterns of the (001)-dominant TiO_2 , (101)-dominant TiO_2 , (001)-dominant Cu-TiO_2 , and (101)-dominant Cu-TiO_2 . SEM images of (b) the (001)-dominant TiO_2 , (c) the (101)-dominant TiO_2 , (d) the (001)-dominant Cu-TiO_2 , and (e) the (101)-dominant Cu-TiO_2 . HRTEM images of (f) the (001)-dominant Cu-TiO_2 with Cu nanoparticles deposited on the (001) facet and (g) the (101)-dominant Cu-TiO_2 with Cu nanoparticles deposited on the (101) facet.

Scanning electron microscopy (SEM) analysis was performed to verify the morphology of the faceted TiO_2 catalysts. As presented in Fig. 1b and c, the (001)-dominant TiO_2 catalysts show a flat sheet morphology, while the (101)-dominant TiO_2 catalysts are truncated octahedral particles. The exposures of (001) facets relative to all facets in the (001)-dominant TiO_2 and (101)-dominant TiO_2 were calculated to be $\sim 70.2\%$ and $\sim 33.2\%$, respectively (details in Fig. S1a–c in ESI†). This means that the (001)-dominant TiO_2 is dominated by (001) facets with an exposure of $\sim 70.2\%$ from its total facets, while the (101)-dominant TiO_2 is dominated by (101) facets with an exposure of $\sim 66.8\%$. The Cu nanoparticles are deposited on both (001) and (101) facets of the (001)-dominant TiO_2 and (101)-dominant TiO_2 , as shown in Fig. 1d and e. The dispersion of the Cu nanoparticles on the surface of the (001)-dominant TiO_2 and the (101)-dominant TiO_2 is further verified using transmission electron microscopy (TEM) analysis. The TEM images with the corresponding energy dispersive X-ray (EDX) mapping show the uniform dispersion of the Cu nano-

particles on the (001)-dominant Cu-TiO_2 and the (101)-dominant Cu-TiO_2 (Fig. S2a–d and Fig. S3a–d in the ESI†). The average size of the Cu nanoparticle was estimated to be 6.65 ± 3.51 nm and 6.81 ± 2.34 nm for the (001)-dominant Cu-TiO_2 and the (101)-dominant Cu-TiO_2 , respectively (Fig. S4a–c and Fig. S5a–d in ESI†). Moreover, the high-resolution TEM (HRTEM) image of the (001)-dominant Cu-TiO_2 shows a Cu nanoparticle anchored on the surface of the (001) facet of the (001)-dominant TiO_2 (Fig. 1f). The lattice fringe of 0.19 nm can be attributed to the (200) and (020) crystal planes of anatase TiO_2 , which are typically correlated with the (001) facet as both (200) and (020) facets have an interfacial angle of 90° between each other on the (001) zone axis diffraction.^{31,44} Meanwhile, the attachment of the Cu nanoparticle is identified by the lattice fringe of 0.20 nm coming from the (111) plane of Cu. We note that a lattice fringe of 0.24 nm coming from Cu_2O (111) is also observed,^{45,46} which indicates the superficial oxidation of Cu metal under an ambient atmosphere.⁴⁷ In addition to the (001) plane, the Cu nanoparticles can also be found on the (101) surface of the (101)-dominant TiO_2 , as presented in Fig. 1g. The lattice fringe of 0.35 nm refers to the (101) plane of the (101)-dominant TiO_2 . Similar to the (001)-dominant Cu-TiO_2 , the crystal planes of both Cu and Cu_2O are also present on the (101)-dominant TiO_2 catalyst.

The chemical states of all catalysts were investigated using X-ray photoelectron spectroscopy (XPS) analysis. As presented in Fig. 2a, the Ti 2p XPS spectra of the (001)-dominant TiO_2 and (001)-dominant Cu-TiO_2 samples show pronounced peaks at 457.3 eV and 462.9 eV, which refer to $\text{Ti}^{4+} 2p_{3/2}$ and $\text{Ti}^{4+} 2p_{1/2}$, respectively.⁴⁸ The same position of the $\text{Ti}^{4+} 2p_{3/2}$ and $\text{Ti}^{4+} 2p_{1/2}$ peaks between the pristine (001)-dominant TiO_2 and (001)-dominant Cu-TiO_2 indicates that there is no significant change in the TiO_2 phase of the (001)-dominant TiO_2 upon depositing Cu nanoparticles. In contrast, the (101)-dominant Cu-TiO_2 shows a shift of the $\text{Ti}^{4+} 2p_{3/2}$ and $\text{Ti}^{4+} 2p_{1/2}$ peaks to lower binding energies (457.4 eV and 463.1 eV, respectively) compared to the pristine (101)-dominant TiO_2 (457.5 eV and 463.2 eV, respectively), as shown in Fig. 2b. The shift of binding energy to lower values suggests the tuned electronic structure of the (101)-dominant TiO_2 upon Cu deposition.^{41,48}

The O 1s XPS spectra are presented in Fig. 2c and d. All catalysts show three deconvoluted peaks at 528.5 eV, 530.8 eV, and 532.3 eV, which can be assigned to the lattice O of TiO_2 , the O ions associated with bridging Ti–OH (OVs), and physisorbed water, respectively.^{41,48} Upon the deposition of the Cu nanoparticles on the surface of the pristine (001)-dominant TiO_2 and (101)-dominant TiO_2 , the intensity of OVs increased, indicating the generation of more OVs. The formation of more OVs in the (001)-dominant Cu-TiO_2 and (101)-dominant Cu-TiO_2 can be correlated with the Cu deposition process, which involves NaBH_4 as a reducing agent.⁴²

The chemical states analysis of the Cu nanoparticles was performed using argon-etched depth profiling XPS to avoid surface oxidation of Cu in air. As presented in Fig. 2e, two pronounced peaks can be observed at 932.03 eV and 951.85 eV in the (001)-dominant Cu-TiO_2 , which can be ascribed to the

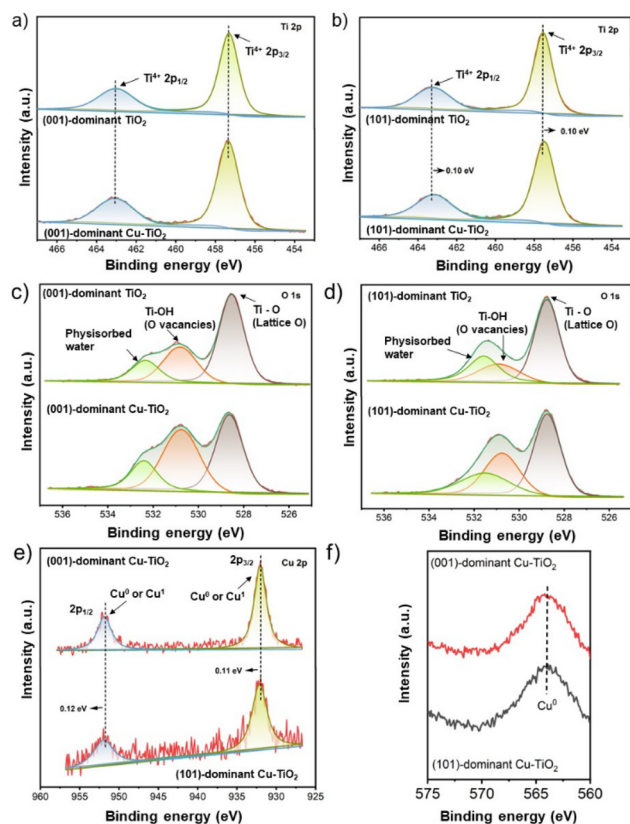


Fig. 2 The Ti 2p XPS spectra of (a) the (001)-dominant TiO_2 and (001)-dominant Cu-TiO_2 , and (b) the (101)-dominant TiO_2 and (101)-dominant Cu-TiO_2 . O 1s XPS spectra of (c) the (001)-dominant TiO_2 and (001)-dominant Cu-TiO_2 , and (d) the (101)-dominant TiO_2 and (101)-dominant Cu-TiO_2 . (e) The Cu 2p XPS spectra of the (001)-dominant Cu-TiO_2 and (101)-dominant Cu-TiO_2 . (f) The Cu LMM AES spectra of the (001)-dominant Cu-TiO_2 and (101)-dominant Cu-TiO_2 .

$2p_{3/2}$ and $2p_{1/2}$ peaks of Cu^+ or Cu^0 .⁴¹ Further analysis using Cu LMM Auger electron spectroscopy (Fig. 2f) confirmed the presence of Cu^0 species in both the (001)-dominant Cu-TiO_2 and (101)-dominant Cu-TiO_2 as indicated by a single peak at 565.2 eV. The presence of single Cu^0 species was also supported by cyclic voltammetry (CV) measurement over freshly prepared (001)-dominant Cu-TiO_2 and (101)-dominant Cu-TiO_2 samples (Fig. S6 in the ESI†), in which both materials do not show reduction peaks correlated to the reduction of Cu^{2+} and Cu^+ , indicating the presence of Cu metal (Cu^0) on the surface of faceted TiO_2 . However, it is worth noting that in the Cu 2p XPS spectrum of the (101)-dominant Cu-TiO_2 (Fig. 2e), the peaks shifted to the higher binding energies of 932.14 eV and 951.97 eV compared to the (001)-dominant Cu-TiO_2 , suggesting lower electron density in the (101)-dominant Cu-TiO_2 resulting from the electron transfer from the Cu nanoparticles to the (101)-dominant TiO_2 support.^{37,41,49}

The above XPS results imply that the electron transfer occurred from the Cu nanoparticles to the (101)-dominant TiO_2 support, which decreased the electron density in the Cu nanoparticles and increased the electron density in the OV

and hence the surrounding Ti atoms. On the other hand, such an electron transfer phenomenon was hardly observed in the (001)-dominant Cu-TiO_2 , which suggests that the Cu nanoparticles have a stronger interaction with (101) facets compared to (001) facets.^{50–52} The electron transfer from Cu to TiO_2 correlates with the presence of the OVs on the surface of TiO_2 . In this regard, OVs can serve as electron trapping centres.^{53,54} Due to the strong interaction between (101) facets of TiO_2 and the Cu nanoparticles, the electrons are transferred from Cu to TiO_2 and pair with singlet electrons in the OVs near the interface.⁵⁵ Additionally, it is also acknowledged that electrons are shallowly trapped in Ti_{5c} on the surface of (101) facets, while electrons are also deeply trapped in Ti_{6c} on the subsurface of (001) facets.³⁴ Therefore, the shallow traps on the surface of Ti_{5c} in (101) facets can provide a more conducive environment for electron mobility, which result in stronger interactions with the Cu nanoparticles.³⁴ To sum up, arising from the strong interaction between the Cu nanoparticles and (101)-dominant TiO_2 support, the electrons transfer from Cu nanoparticles to the OVs in (101) facets, leading to electron-deficient Cu nanoparticles.^{39,41,49}

Electrocatalytic NO_3^- RR evaluation

An electrocatalytic activity test of faceted- TiO_2 -based catalysts was performed in an H-type cell with a typical three-electrode configuration using a Nafion 117 membrane to separate the cathode and the anode chambers. The prepared catalysts were dropcast on carbon paper substrates as the working electrodes ($1.0 \text{ mg}_{\text{cat}} \text{ cm}^{-2}$, details in the Experimental section). Prior to the NO_3^- RR test, the prepared electrodes were initially examined using linear sweep voltammetry (LSV) from +0.1 V to −1.2 V vs. RHE in 0.5 M Na_2SO_4 solution with and without the addition of 50 ppm NO_3^- -N. The LSV curves of both the pristine (001)-dominant TiO_2 and (101)-dominant TiO_2 electrodes showed a slight increase in current density upon the addition of NO_3^- (Fig. S7 in the ESI†), while the increase in current density was apparently exaggerated with the deposition of Cu nanoparticles (Fig. 3a and b).¹⁹ Besides, the corresponding onset potential of the LSV curves for both faceted- TiO_2 electrodes also shifted to the less negative value (−0.3 V vs. RHE) with the deposition of Cu nanoparticles. Note that the increase of the current density for the (101)-dominant Cu-TiO_2 is greater than that of the (001)-dominant Cu-TiO_2 , suggesting the stronger promoting effect in the NO_3^- RR upon Cu deposition on the (101) facet of the (101)-dominant TiO_2 .

The electrocatalytic NO_3^- RR performances were further examined using chronoamperometry (i - t) tests at different applied potentials in 0.5 M NaSO_4 containing 50 ppm NO_3^- -N. The concentration levels of NO_3^- , NH_3 , and NO_2^- were determined using spectrophotometric methods (Fig. S8a–c in the ESI†).⁵⁶ The NO_3^- conversion rate increased along with the more negative potentials (Fig. S9 in the ESI†). The effect of Cu deposition on the NO_3^- conversion can be observed clearly at the potentials of −0.8 and −0.9 V vs. RHE, where both the (001)-dominant Cu-TiO_2 and (101)-dominant Cu-TiO_2 show

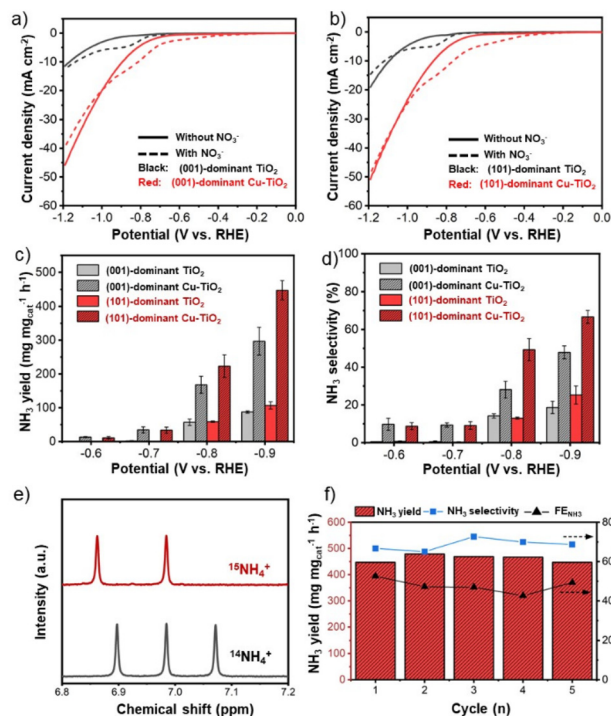


Fig. 3 LSV curves of (a) the (001)-dominant TiO₂ and (001)-dominant Cu-TiO₂, and (b) the (101)-dominant TiO₂ and (101)-dominant Cu-TiO₂ in 0.5 M Na₂SO₄ without and with the addition of 50 ppm NO₃⁻-N. (c) NH₃ yield and (d) NH₃ selectivity. All catalytic activity experiments were performed in 0.5 M Na₂SO₄ containing 50 ppm NO₃⁻-N. (e) ¹H NMR spectra of the electrolyte after the electrocatalytic reduction reaction using ¹⁵NO₃⁻ and ¹⁴NO₃⁻ as the nitrogen sources. The reaction for isotope labelling was performed for the (101)-dominant Cu-TiO₂ at -0.9 V vs. RHE in 0.5 M Na₂SO₄ containing 50 ppm NO₃⁻-N. (f) Stability test of the (101)-dominant Cu-TiO₂ was performed at -0.9 V vs. RHE in 0.5 M Na₂SO₄ containing 50 ppm NO₃⁻-N.

higher NO₃⁻ conversion rates compared to the pristine TiO₂ counterparts.

Moreover, an obvious trend related to the effect of Cu deposition on the different facets of TiO₂ can be observed in the NH₃ yield rate (Fig. 3c). Within all the applied potentials, both the (001)-dominant Cu-TiO₂ and the (101)-dominant Cu-TiO₂ showed significantly higher NH₃ yield rates compared to the pristine (001)-dominant TiO₂ and (101)-dominant TiO₂. The activity increased more significantly along with the more negative potentials, reaching the highest value at -0.9 V vs. RHE with NH₃ yields of 296.6 μg mg_{cat}⁻¹ h⁻¹ and 447.5 μg mg_{cat}⁻¹ h⁻¹ for the (001)-dominant Cu-TiO₂ and the (101)-dominant Cu-TiO₂, respectively. The NH₃ yield rate of the (101)-dominant Cu-TiO₂ is 4.2 times higher than that of the pristine (101)-dominant TiO₂ (106.7 μg mg_{cat}⁻¹ h⁻¹), while the NH₃ yield of the (001)-dominant Cu-TiO₂ is only 3.3 times higher than the pristine counterpart (87.9 μg mg_{cat}⁻¹ h⁻¹). Therefore, the (101)-dominant Cu-TiO₂ exhibits an exaggerated NH₃ yield increase compared to the (001)-dominant Cu-TiO₂. Similar trends can also be observed in the corresponding NH₃ selectivity (Fig. 3d) and FE_{NH₃} (Fig. S10 in the ESI[†]). The highest NH₃

selectivity value was achieved at -0.9 V with values of 66.7% and 47.8% for the (101)-dominant Cu-TiO₂ and the (001)-dominant Cu-TiO₂, respectively. Additionally, it is worth noting that FE_{NH₃} shows a volcano plot with the highest values being reached at -0.8 V vs. RHE with values of 67.1% and 47.0% for the (101)-dominant Cu-TiO₂ and the (001)-dominant Cu-TiO₂, respectively. Note that the NH₃ selectivity value was calculated based on the concentration change of NO₃⁻ only with the corresponding products, while the FE was calculated based on the total current regardless of the reactions (details in the ESI[†]). Therefore, the calculation of the NH₃ selectivity value excluded the contribution of the hydrogen evolution reaction (HER), while the FE_{NH₃} took it into consideration.^{19,57} The decrease of the FE_{NH₃} for all electrodes at -0.9 V vs. RHE is attributed to the intensified HER, as evidenced by the significant increase of the FE_{H₂} (Fig. S11 in the ESI[†]).^{14,19} Accordingly, both the NO₂⁻ selectivity and the FE_{NO₂} also decreased at -0.9 V vs. RHE (Fig. S12 and Fig. S13 in the ESI[†]). Another possible byproduct, *i.e.*, hydrazine (N₂H₄), was also detected using the Watt and Chrisp method (detailed in the Experimental section in the ESI[†]). In all catalytic reactions, no hydrazine (N₂H₄) was detected as presented in Fig. S14a-c in the ESI[†] excluding the possibility of N₂H₄ as a byproduct. We note that the greatest performance exhibited by the (101)-dominant Cu-TiO₂ catalyst in this work is, in fact, on a par with previous studies reported in the literature, specifically for Ti-based and Cu⁰-based catalysts in neutral media (Table S1 in the ESI[†]). However, it is worth noting that the exhibited performances in this work resulted from lower external potentials (-0.9 V vs. RHE) compared to the other Ti-based catalysts (-1.0 to -1.6 V vs. RHE), which is also one of the important parameters for evaluating the electrocatalytic performance.^{58,59}

Control experiments were then performed to verify the origin of the produced NH₃. As presented in Fig. 3e, the electrolyte taken from the electrocatalytic reduction of Na¹⁵NO₃ shows typical doublet peaks at δ = 6.86 and δ = 6.98 ppm, while the triplet peak was observed in the spectra when employing Na¹⁴NO₃. These ¹⁵N isotope-labelling results strongly confirm that the produced NH₃ originated from the electroreduction of NO₃⁻.^{19,56} Moreover, a negligible amount of NH₃ produced in the absence of NO₃⁻ and at the open circuit potential (OCP) further supports the results from ¹⁵N isotope-labelling experiments (Fig. S15 in the ESI[†]). No accumulation of NH₃ was observed upon exposing the electrolyte to the air, excluding possible NH₃ contamination from the environment (Fig. S16 in the ESI[†]).

The exaggerated improvement in the NH₃ yield rate and NH₃ selectivity can be correlated with the strong metal-support interaction exhibited by the (101)-dominant Cu-TiO₂ catalyst. On the other hand, we note that the concentration of OV also increases in both the (001)-dominant TiO₂ and (101)-dominant TiO₂ upon Cu deposition as indicated by the O 1s XPS spectra in Fig. 2c and d. One of the oxygen (O) atoms in NO₃⁻ can occupy the OV and coordinate with the surrounding Ti³⁺ of TiO₂, which weakens the N-O bonding for better activation.¹⁸ Therefore, to investigate the contribution of OVs, we

also performed the electrocatalytic test on the reduced-(001)-dominant TiO_2 and reduced-(101)-dominant TiO_2 prepared by the NaBH_4 reduction method on the pristine faceted TiO_2 without the addition of Cu salts. As verified by the electron paramagnetic resonance (EPR) spectra of the pristine (101)-dominant TiO_2 and the reduced (101)-dominant TiO_2 (Fig. S17 in the ESI†), the reduced (101)-dominant TiO_2 shows a slightly higher peak intensity at $g = 2.003$, indicating a higher concentration of OV's upon implementing the NaBH_4 reduction process.⁴⁸ Moreover, as presented in Fig. S18a–d in the ESI†, the reduced-(001)-dominant TiO_2 and the reduced-(101)-dominant TiO_2 also show slight increases in NH_3 yield rate and selectivity, suggesting the benefits of OV's generation in the NO_3^- RR to a certain degree.¹⁸ However, the improved performances by the reduced-faceted- TiO_2 electrodes are much less significant compared to the enhancements exhibited by the Cu-loaded faceted TiO_2 electrodes.

To further investigate the contribution from the Cu nanoparticles, which serve as the co-catalyst in the Cu-loaded TiO_2 electrode, we also performed electrocatalytic tests over Cu nanoparticles prepared using the NaBH_4 reduction method. For this purpose, we deposited an equal amount of Cu nanoparticles contained in the (001)-dominant Cu- TiO_2 and (101)-dominant Cu- TiO_2 electrodes. As presented in Fig. S19 in the ESI†, Cu nanoparticles show activity for NO_3^- reduction to NH_3 .⁶⁰ NH_3 yield rates increase along with the more negative potentials. However, the magnitude of the NH_3 yield rate is much inferior compared to that of the Cu-loaded faceted TiO_2 catalysts. These control experiments provide evidence that significant enhancement of the NH_3 yield rate, selectivity, and FE_{NH_3} over the (001)-dominant Cu- TiO_2 and the (101)-dominant Cu- TiO_2 is mainly determined by the interaction between the Cu nanoparticles and the faceted TiO_2 . Moreover, the stronger metal-support interaction between the Cu nanoparticles and the (101) facets of TiO_2 further enhance the performance. The presumption can be derived from the fact that the increase in NH_3 yield rate and selectivity is exaggerated for the (101)-dominant Cu- TiO_2 compared to the (001)-dominant Cu- TiO_2 . Moreover, the (101)-dominant Cu- TiO_2 shows a stable NH_3 yield rate, NH_3 selectivity, and FE_{NH_3} in five consecutive reactions (Fig. 3f), suggesting the appreciable stability of the designed system for the NO_3^- RR.

Mechanism study

Time-dependent experiments were performed to understand the kinetics and reaction mechanism of the NO_3^- RR (Fig. 4a–d). For all prepared catalysts, the NO_3^- concentration decreases over time accompanied by the increase in NH_3 and NO_2^- concentrations. The apparent reduction rate constant values of NO_3^- calculated based on the Langmuir–Hinshelwood model for the (101)-dominant Cu- TiO_2 ($k_{\text{ap}} = 0.00551 \text{ min}^{-1}$) and the (001)-dominant Cu- TiO_2 ($k_{\text{ap}} = 0.00476 \text{ min}^{-1}$) are higher than those of the pristine (101)-dominant TiO_2 ($k_{\text{ap}} = 0.00368 \text{ min}^{-1}$) and (001)-dominant TiO_2 ($k_{\text{ap}} = 0.00322 \text{ min}^{-1}$) counterparts, suggesting the positive role of Cu deposition in promoting the NO_3^- RR (Fig. S20a and b in the ESI†).^{38,61,62}

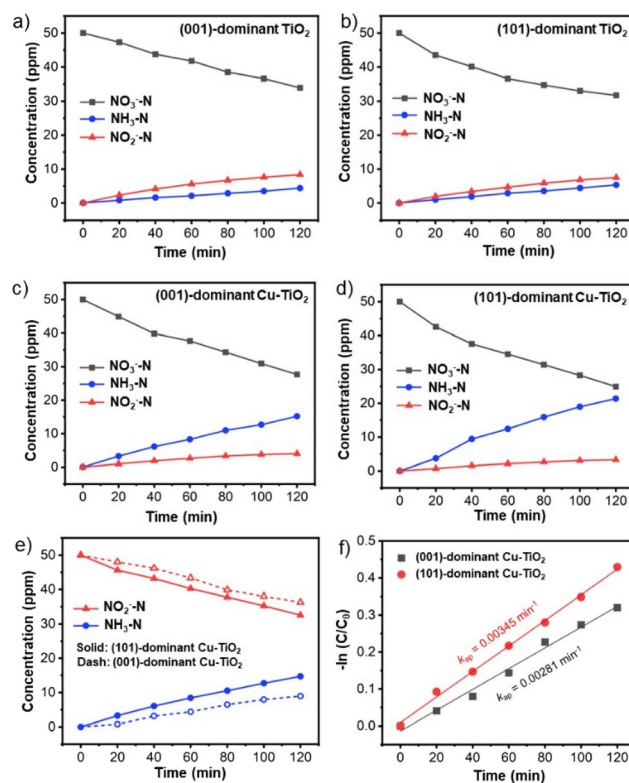


Fig. 4 NO_3^- , NH_3 , and NO_2^- concentration changes over (a) the (001)-dominant TiO_2 , (b) the (101)-dominant TiO_2 , (c) the (001)-dominant Cu- TiO_2 , and (d) the (101)-dominant Cu- TiO_2 . All experiments were performed at -0.9 V vs. RHE in $0.5 \text{ M Na}_2\text{SO}_4$ containing 50 ppm of NO_3^- -N for 2 h . NO_2^- and NH_3 concentration changes over the (001)-dominant Cu- TiO_2 and the (101)-dominant Cu- TiO_2 , and (f) the corresponding Langmuir–Hinshelwood plots. All the experiments were performed at -0.9 V vs. RHE in $0.5 \text{ M Na}_2\text{SO}_4$ containing 50 ppm of NO_2^- -N for 2 h .

The apparent activation energy (E_a) also decreases upon Cu loading on the surface of faceted TiO_2 . The E_a for the (101)-dominant Cu- TiO_2 is significantly lower ($E_a = 4.61 \text{ kJ mol}^{-1}$) than that of the pristine (101)-dominant TiO_2 ($E_a = 15.79 \text{ kJ mol}^{-1}$). The same trend can be observed in the (001)-dominant Cu- TiO_2 ($E_a = 13.90 \text{ kJ mol}^{-1}$) and the (001)-dominant TiO_2 ($E_a = 24.03 \text{ kJ mol}^{-1}$) (Fig. S21a and b in the ESI†).^{63,64} It is noteworthy that among the four samples, the (101)-faceted TiO_2 -based catalysts typically show lower apparent E_a values than the (001)-faceted TiO_2 -based catalysts, indicating the advantage of (101) facet exposure and Cu loading on these facets for reducing the E_a . These E_a values agree well with the Tafel plots (Fig. S22 in the ESI†), in which the (101)-dominant Cu- TiO_2 shows a lower Tafel slope ($178.7 \text{ mV dec}^{-1}$) than the (001)-dominant Cu- TiO_2 (203.7 mV), indicating the higher kinetics rate of the former for the electrocatalytic NO_3^- RR.^{65,66} These apparent E_a values and the Tafel slopes are in good agreement with the reduction rate (Fig. 4a–d and Fig. S20a, b in the ESI†), as mentioned before. In addition to the kinetics information, the higher reduction rate of the (101)-dominant Cu- TiO_2 suggests a higher adsorption strength between the NO_3^- ions with the catalyst surface. This assumption can be rationalized

based on the presence of the electron-deficient Cu nanoparticles in the (101)-dominant Cu-TiO₂, which are more conducive to attracting the negatively charged NO₃[−] ions.^{38,39} This attraction could also lead to the accumulation of NO₃[−] near the catalyst surface, which facilitates the contact between the NO₃[−] ions and the surface OVs in the surrounding Cu nanoparticles.³⁹

The influence of the strong metal-support interaction on the catalysis process can be observed by the product distribution, specifically the evolution of NH₃ and NO₂[−] as the two major products. As shown in Fig. 4a and b, the (001)-dominant TiO₂ and the (101)-dominant TiO₂ electrodes show that NO₂[−] is the dominant product at −0.9 V vs. RHE. On the other hand, upon the deposition of Cu on the faceted TiO₂, NH₃ emerges as the dominant product from the beginning of the reaction (Fig. 4c and d). Notably, the increase in the NH₃ concentration of the (101)-dominant Cu-TiO₂ is much higher than that of the (001)-dominant Cu-TiO₂, which is in good agreement with the trends of NH₃ yield rate and NH₃ selectivity in the catalytic test. The time-dependent experiments in a prolonged reaction period show similar trends for the concentration changes of the NO₃[−] reactant and the reduction products (Fig. S23a and b in the ESI†). The greater increase in NH₃ production of the (101)-dominant Cu-TiO₂ indicates the benefit of the strong metal-support interaction between the Cu nanoparticles and (101) facets of TiO₂ in promoting the selective NO₃[−]RR to NH₃.

We note that the detection of NO₂[−] in the electrolyte during the NO₃[−]RR indicates that the production rate of NO₃[−] to *NO₂ is faster than that of NO₂[−] to NH₃, and thus leads to the desorption of *NO₂ from the catalyst surface into the electrolyte.⁶⁰ The detection of higher amounts of NO₂[−] in the electrolyte may also indicate that the binding strength of *NO₂ to the catalyst surface is weaker, hence it can easily be desorbed from the catalyst surface into the electrolyte. Therefore, to further investigate the role of the *NO₂ intermediate in the NO₃[−]RR, time-dependent NO₂[−] reduction reactions (NO₂[−]RRs) over the (001)-dominant Cu-TiO₂ and the (101)-dominant Cu-TiO₂ catalysts were performed. As presented in Fig. 4e, the decrease in the NO₂[−] concentration using the (001)-dominant Cu-TiO₂ is slower than that using the (101)-dominant Cu-TiO₂. The corresponding apparent rate constant values based on the Langmuir-Hinshelwood model of the (101)-dominant Cu-TiO₂ and the (001)-dominant Cu-TiO₂ are 0.00345 min^{−1} and 0.00281 min^{−1} (Fig. 4f), respectively.^{61,67} The higher rate constant of NO₂[−] reduction may indicate the higher binding strength between NO₂[−] and the surface of the (101)-dominant Cu-TiO₂ when forming *NO₂. These results agree well with the lower amount of NO₂[−] produced using the (101)-dominant Cu-TiO₂ compared with that produced using the (001)-dominant Cu-TiO₂ in the NO₃[−]RR (Fig. S24 in the ESI†). Based on these findings, the exaggerated enhancement in the NH₃ production by the (101)-dominant Cu-TiO₂ can also be attributed to the stronger binding strength of *NO₂, which suppresses the desorption of *NO₂ into the electrolyte and subsequently promotes the subsequent hydrogenation process.

The intrinsic electrochemical properties of the prepared electrodes are important factors in influencing catalytic performance. Therefore, electrochemical impedance spectroscopy (EIS), electrochemical active surface area (ECSA) analysis, and Mott-Schottky analysis were performed for the pristine and Cu-deposited TiO₂ electrodes. The Nyquist plots of the Cu-deposited TiO₂ electrodes show smaller arc radii than the pristine counterparts (Fig. 5a and b). The series resistance (*R*_s), which is correlated with the resistance from the solution, is comparable among all the electrodes (Table S2 in the ESI†).^{61,68,69} On the other hand, the charge transfer resistance (*R*_{CT}) decreases significantly upon Cu deposition. The *R*_{CT} value of the (001)-dominant Cu-TiO₂ (27.20 Ω) is 2.7 times lower than that of the pristine (001)-dominant TiO₂ (74.38 Ω). Meanwhile, the (101)-dominant Cu-TiO₂ shows a more significant decrease in the *R*_{CT} value (40.28 Ω), which is 3.8 times lower than that of the pristine (101)-dominant TiO₂ (152.50 Ω). The more efficient electron transfer as evidenced by the higher decrease in the *R*_{CT} value on the (101)-dominant Cu-TiO₂ than on the (001)-dominant Cu-TiO₂ is likely contributed to by the stronger interaction between Cu nanoparticles and (101) facets of TiO₂ in the (101)-dominant Cu-TiO₂.^{41,70} The ECSA was further investigated by measuring the electrochemical double-layer capacitance (*C*_{dl}), which is proportional to the ECSA. The linear fitting of the charging current density with various scan rates (Fig. 5c and d and Fig. S25a–d in the ESI†) reveals that the *C*_{dl} values of the (001)-dominant Cu-TiO₂ (*C*_{dl} = 0.0601 mF cm^{−2}) and the (101)-dominant Cu-TiO₂ (*C*_{dl} = 0.0886 mF cm^{−2}) are higher than those of the pristine (001)-dominant TiO₂ (*C*_{dl} = 0.0546 mF cm^{−2}) and the (101)-dominant TiO₂ (*C*_{dl} = 0.0685 mF cm^{−2}), suggesting that more active sites are present in the Cu-deposited TiO₂ catalysts.⁴¹ Moreover, the Mott-Schottky plots show positive slopes for all the electrodes, indi-

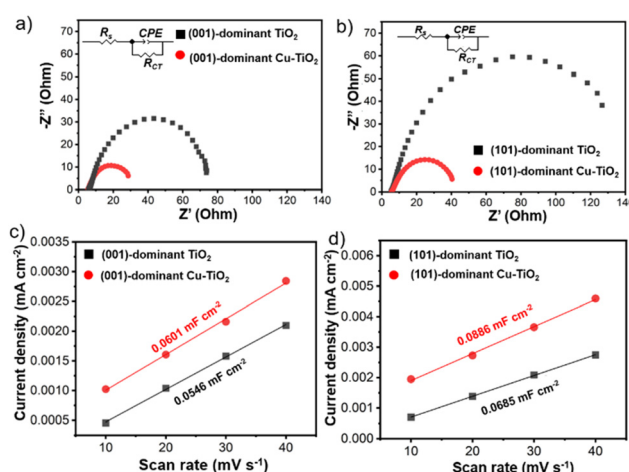


Fig. 5 Nyquist plots of (a) the (001)-dominant TiO₂ and (001)-dominant Cu-TiO₂ and (b) the (101)-dominant TiO₂ and (101)-dominant Cu-TiO₂. The insets are the equivalent electrical circuits. Charging current density plotted against the scan rate at 0.655 V vs. RHE for (c) the (001)-dominant TiO₂ and (001)-dominant Cu-TiO₂, and (d) the (101)-dominant TiO₂ and (101)-dominant Cu-TiO₂.

cating the n-type nature of the faceted-TiO₂ electrodes (Fig. S26a and b in the ESI†).^{41,71} The (001)-dominant Cu-TiO₂ and the (101)-dominant Cu-TiO₂ show smaller slopes compared with those of the pristine (001)-dominant TiO₂ and (101)-dominant TiO₂, also indicating the higher donor density in the Cu-deposited TiO₂.⁷² These results suggest that the significant enhancement in NH₃ production exhibited by the (101)-dominant Cu-TiO₂ is likely contributed to by the promoted electron transfer. In this regard, the nature of (101) facets, which possess shallow traps on the surface of Ti_{5c} in (101) facets, can provide a more conducive environment for electron mobility as reported in the literature.³⁴

The above electrocatalytic NO₃[−]RR activities, time-dependent experiments, and electrochemical analysis have collectively suggested that (1) the Cu deposition on the faceted-TiO₂ surface leads to higher NH₃ production, NH₃ selectivity, and FE_{NH₃} and (2) the deposition of Cu on the (101) facet is more beneficial for promoting NH₃ production compared to Cu deposition on the (001) facet due to the stronger interaction between the Cu nanoparticles and the dominant (101) facet in the (101)-dominant Cu-TiO₂. The Cu metal was previously reported as an active catalyst for the NO₃[−]RR in the literature.^{62,73–75} The activity originates from the d-orbital electronic configuration of Cu, where the NO₃[−] reactant binds with Cu by electron donation from the highest occupied molecular orbital (HOMO) of NO₃[−] to the empty orbital of Cu accompanied by the backdonation from the fully occupied d orbital to the lowest unoccupied molecular orbital (LUMO) of NO₃[−].⁶⁰ Therefore, in addition to OVs as active sites, the deposited Cu nanoparticles can also serve as active sites in the (001)-dominant Cu-TiO₂ and the (101)-dominant Cu-TiO₂ catalysts, resulting in significantly higher NH₃ production than that from the pristine counterparts. Additionally, due to the strong interaction between the Cu nanoparticles and (101) facets of TiO₂, the electrons are transferred from the Cu nanoparticles to the (101) facets of TiO₂ resulting in electron-deficient Cu, which can strongly attract and accumulate the negatively charged NO₃[−].³⁹ The stronger absorption strength is also found in the NO₂[−] (and *NO₂), which suppresses the desorption of *NO₂ to the electrolyte. Finally, the exposure of (101) facets of TiO₂, possessing shallow traps for electrons on the Ti_{5c} surface could provide a more conducive environment for electron mobility, thus promoting the electron transfer in the (101)-dominant Cu-TiO₂ resulting in significant enhancements in NH₃ production and NH₃ selectivity over the (101)-dominant Cu-TiO₂ catalyst.

Conclusions

In conclusion, the strong interaction between the deposited Cu nanoparticles and the TiO₂ support with the dominant (101) facet exposure promoted selective NH₃ production from the NO₃[−]RR. The (101)-dominant Cu-TiO₂ catalyst demonstrated the highest NH₃ yield rate of 447.5 μg mg_{cat}^{−1} h^{−1} at −0.9 V vs. RHE, which is 4.2 times higher than that of the pris-

tine (101)-dominant TiO₂ catalyst with an NH₃ yield of 106.7 μg mg_{cat}^{−1} h^{−1}. In comparison, the (001)-dominant Cu-TiO₂ counterpart showed NH₃ yield rate of 296.6 μg mg_{cat}^{−1} h^{−1} under identical reaction conditions, which is 3.3 times higher than that of the pristine (001)-dominant TiO₂ with an NH₃ yield of 87.9 μg mg_{cat}^{−1} h^{−1}. The greater increase in catalytic performance for the (101)-dominant TiO₂ with Cu deposition was ascribed to the formation of electron-deficient Cu nanoparticles, the stronger binding energy of *NO₂, and the promoted electron transfer originating from the strong interaction between the Cu nanoparticles and (101) facets of TiO₂. Collectively, these factors suppressed the *NO₂ desorption and promoted the subsequent hydrogenation process, leading to direct NO₃[−] reduction to NH₃. These findings can stimulate the future surface design over other oxide supports toward the efficient electrocatalytic NO₃[−]RR to produce NH₃.

Experimental

The experimental details are provided in the ESI† This section summarizes the material synthesis, characterization, and electrochemical measurements.

Preparation of the (001)-dominant TiO₂ (flat sheet) and the (101)-dominant TiO₂ (truncated octahedral)

The TiO₂ samples with different dominant facets were prepared using the hydrothermal method with NaF as a capping agent, as reported by Mikrut *et al.*⁴⁰ In a typical procedure for preparing (001)-dominant TiO₂, 532 mg NaF was mixed with 160 mL of HCl (12.8%). The mixture was then stirred to form a clear solution. Subsequently, 781.6 mg of TiOSO₄ was added to the solution, followed by constant stirring for 1 h to form a clear solution. The resulting solution was then placed into a 200 mL Teflon-lined stainless-steel autoclave and was heated at 180 °C for 12 h. After naturally cooling down to room temperature, the powders were collected and centrifuged in water and ethanol several times. The obtained powders were then dried at 60 °C in a vacuum oven for 12 h and calcined at 600 °C for 2 h at a heating rate of 2 °C min^{−1} under an argon atmosphere (20 mL min^{−1}). The (101)-dominant TiO₂ (truncated octahedral) was prepared using the same method as that of the (001)-dominant TiO₂ by adjusting the concentration of HCl (6.7%), the mass of NaF (279.6 mg), and the amount of TiOSO₄ (390.8 mg).

Copper (Cu) deposition on (001)-dominant TiO₂ and (101)-dominant TiO₂

The Cu deposition was performed using NaBH₄ as a reducing agent.⁴¹ 20 mg of the (001)-dominant TiO₂ or the (101)-dominant TiO₂ was dispersed in 15 mL of DI water, followed by sonication for 30 min. After sonication, 315 μL of 20 mM Cu (NO₃)₂·3H₂O solution was added slowly under vigorous stirring. The stirring was continued for 30 min. 30 mg of NaBH₄ was then added, and the stirring was continued for another 20 min. The powders were subsequently separated by centrifugation.

gation and washed using excess deionized water and ethanol. The powders were finally dried in a vacuum oven at 60 °C for 12 h.

Characterization

The crystal phase of each prepared sample was analyzed using an X-ray diffraction (XRD) PANalytical X'pert³ powder X-ray diffractometer operated at 40 kV and 100 mA with Cu K α radiation. The morphology and the composition of the catalyst were observed using a transmission electron microscope (TEM) FEI Tecnai F20 and scanning electron microscope (SEM) Zeiss EVO 10. The oxidation states of Ti, Cu, and O elements were characterized using X-ray photoelectron spectroscopy (XPS, Thermo Scientific NEXSA) conducted with an Al K α X-ray excitation source. All binding energies were referenced to the C 1s peak at 283.67 eV. Electron paramagnetic resonance (EPR) analysis was performed using a Bruker EMXPLUS EPR instrument (Germany). The amount of deposited metal was measured using inductively coupled plasma optical emission spectroscopy (ICP-OES, Optima 8000). The ultraviolet-visible (UV-vis) absorbance data were collected on a Shimadzu UV-3600 UV spectrophotometer.

Electrochemical measurements

The prepared samples were dropcast on pieces of carbon paper as the working electrodes. Before the drop-casting, the pieces of carbon paper were washed in a mixture of methanol and acetone (1:1; v/v) and ultrasonicated for 10 min. Subsequently, the pieces of carbon paper were washed again in water and ultrasonicated for another 10 min. The pieces of carbon paper were then dried at room temperature. Meanwhile, 10 mg of TiO₂ powders, *e.g.*, the (001)-dominant TiO₂, were mixed with 0.24 mL of water and 0.72 mL of ethanol. After that, 0.04 mL of Nafion solution (5%) was added. The mixture was then ultrasonicated for 1 h to form a homogeneous suspension. 0.1 mL of the prepared homogeneous suspension was then dropped onto 1.0 × 1.0 cm² carbon paper (1.0 mg_{cat} cm⁻²). The same procedure was applied to prepare the electrodes loaded with the other catalysts (*i.e.*, the (101)-dominant TiO₂, (001)-dominant Cu-TiO₂, and (101)-dominant Cu-TiO₂).

The electrochemical measurements were carried out using a CHI 660 instrument in an H-type cell using the TiO₂ based-thin film electrode as the working electrode, saturated calomel electrode (SCE) as the reference electrode, and platinum foil as the counter electrode. The surface area of the working electrode was controlled within 1.0 × 1.0 cm². 0.5 M Na₂SO₄ was used as the electrolyte. The electrolyte volumes in the anodic and cathodic chambers were 30 and 40 mL, respectively. A Nafion 117 membrane was placed between the anodic and cathodic chambers. The catholyte was purged with Ar at a flow rate of 50 mL min⁻¹ for 15 min under vigorous stirring. Before the NO₃⁻RR measurement, cyclic voltammetry (CV) was performed from +0.1 V to -1.2 V *vs.* RHE to reach a stable curve. After the CV, NaNO₃ (50 ppm NO₃⁻-N) was added to the cathode chamber. The chronoamperometry (*i-t*) test was

carried out at different potentials for 2 h at a stirring rate of 300 rpm. All potentials were referenced to reversible hydrogen electrode (RHE) by the Nernst equation ($E_{\text{RHE}} = E_{\text{SCE}} + 0.059 \times \text{pH} + 0.241$).

To investigate the electrochemically active surface area (ECSA), the working electrode was cycled in the non-faradaic potential region at various scan rates from 10 to 40 mV s⁻¹ in 0.5 M Na₂SO₄. By plotting the charging current density against the scan rate, the double-layer capacitance (C_{dl}) was calculated by determining the slope value. Electrochemical impedance spectroscopy (EIS) was performed at the potential of -0.7 V *vs.* RHE at a frequency of 10⁻¹–10⁵ Hz and amplitude of 5 mV. Mott-Schottky plots were recorded at a frequency of 0.5 kHz and amplitude of 0.01 V.

Conflicts of interest

There are no conflicts to declare.

Acknowledgements

This project was financially supported by the Hong Kong Research Grant Council (RGC) General Research Fund (GRF) CityU 11306920, CityU 11308721, and CityU 11316522. The authors acknowledge the financial support by the Science and Technology Development Fund, Macao SAR (File No. FDCT-0125/2022/A), and the National Natural Science Foundation of China (22305009).

References

- 1 L. Wang, M. Xia, H. Wang, K. Huang, C. Qian, C. T. Maravelias and G. A. Ozin, *Joule*, 2018, **2**, 1055–1074.
- 2 B. M. Comer, P. Fuentes, C. O. Dimkpa, Y.-H. Liu, C. A. Fernandez, P. Arora, M. Realff, U. Singh, M. C. Hatzell and A. J. Medford, *Joule*, 2019, **3**, 1578–1605.
- 3 L. Hollevoet, F. Jardali, Y. Gorbanev, J. Creel, A. Bogaerts and J. A. Martens, *Angew. Chem., Int. Ed.*, 2020, **59**, 23825–23829.
- 4 D. W. Kim, D. W. Kang, M. Kang, J.-H. Lee, J. H. Choe, Y. S. Chae, D. S. Choi, H. Yun and C. S. Hong, *Angew. Chem., Int. Ed.*, 2020, **59**, 22531–22536.
- 5 W. P. Utomo, M. K. H. Leung, Z. Yin, H. Wu and Y. H. Ng, *Adv. Funct. Mater.*, 2022, **32**, 2106713.
- 6 A. J. Martín, T. Shinagawa and J. Pérez-Ramírez, *Chem*, 2019, **5**, 263–283.
- 7 S. Lin, X. Zhang, L. Chen, Q. Zhang, L. Ma and J. Liu, *Green Chem.*, 2022, **24**, 9003–9026.
- 8 C. J. M. van der Ham, M. T. M. Koper and D. G. H. Hetterscheid, *Chem. Soc. Rev.*, 2014, **43**, 5183–5191.
- 9 O. Elishav, B. M. Lis, E. M. Miller, D. J. Arent, A. Valera-Medina, A. G. Dana, G. E. Shter and G. S. Grader, *Chem. Rev.*, 2020, **120**, 5352–5436.

- 10 L. Barrera and R. Bala Chandran, *ACS Sustainable Chem. Eng.*, 2021, **9**, 3688–3701.
- 11 T. A. Belay, F. M. Lin, C. Y. Lin, H. M. Hsiao, M. F. Chang and J. C. Liu, *Water Sci. Technol.*, 2015, **72**, 960–965.
- 12 X. Zhang, Y. Wang, C. Liu, Y. Yu, S. Lu and B. Zhang, *Chem. Eng. J.*, 2021, **403**, 126269.
- 13 Y. Li, Y. K. Go, H. Ooka, D. He, F. Jin, S. H. Kim and R. Nakamura, *Angew. Chem., Int. Ed.*, 2020, **59**, 9744–9750.
- 14 X. Wan, W. Guo, X. Dong, H. Wu, X. Sun, M. Chu, S. Han, J. Zhai, W. Xia, S. Jia, M. He and B. Han, *Green Chem.*, 2022, **24**, 1090–1095.
- 15 Y. Wang, L. Zhang, Y. Niu, D. Fang, J. Wang, Q. Su and C. Wang, *Green Chem.*, 2021, **23**, 7594–7608.
- 16 Y.-T. Xu, K.-C. Ren, Z.-M. Tao, D. K. Sam, E. Feng, X. Wang, G. Zhang, J. Wu and Y. Cao, *Green Chem.*, 2023, **25**, 589–595.
- 17 A. Stirling, I. Pápai, J. Mink and D. R. Salahub, *J. Chem. Phys.*, 1994, **100**, 2910–2923.
- 18 R. Jia, Y. Wang, C. Wang, Y. Ling, Y. Yu and B. Zhang, *ACS Catal.*, 2020, **10**, 3533–3540.
- 19 Y. Wang, W. Zhou, R. Jia, Y. Yu and B. Zhang, *Angew. Chem., Int. Ed.*, 2020, **59**, 5350–5354.
- 20 R. Daiyan, T. Tran-Phu, P. Kumar, K. Iputera, Z. Tong, J. Leverett, M. H. A. Khan, A. A. Esmailpour, A. Jalili, M. Lim, A. Tricoli, R.-S. Liu, X. Lu, E. Lovell and R. Amal, *Energy Environ. Sci.*, 2021, **14**, 3588–3598.
- 21 J. Fu, F. Yao, T. Xie, Y. Zhong, Z. Tao, S. Chen, L. He, Z. Pi, K. Hou, D. Wang, X. Li and Q. Yang, *Sep. Purif. Technol.*, 2021, **276**, 119329.
- 22 D. R. MacFarlane, P. V. Cherepanov, J. Choi, B. H. R. Suryanto, R. Y. Hodgetts, J. M. Bakker, F. M. F. Vallana and A. N. Simonov, *Joule*, 2020, **4**, 1186–1205.
- 23 G. Liu, H. G. Yang, J. Pan, Y. Q. Yang, G. Q. (Max) Lu and H.-M. Cheng, *Chem. Rev.*, 2014, **114**, 9559–9612.
- 24 Z. Xiong, Z. Lei, Y. Li, L. Dong, Y. Zhao and J. Zhang, *J. Photochem. Photobiol., C*, 2018, **36**, 24–47.
- 25 B. Shao, W. Zhao, S. Miao, J. Huang, L. Wang, G. Li and W. Shen, *Chin. J. Catal.*, 2019, **40**, 1534–1539.
- 26 Z. Xie, H. L. Tan, H. Wu, R. Amal, J. Scott and Y. H. Ng, *Mater. Today Energy*, 2022, **26**, 100986.
- 27 H. L. Tan, X. Wen, R. Amal and Y. H. Ng, *J. Phys. Chem. Lett.*, 2016, **7**, 1400–1405.
- 28 J. Chen, X. Li, B. Lei, L. Zhou and S. Wang, *Green Chem.*, 2019, **21**, 483–490.
- 29 J. Pan, G. Liu, G. Q. (Max) Lu and H.-M. Cheng, *Angew. Chem., Int. Ed.*, 2011, **50**, 2133–2137.
- 30 W. Wang, J. Fang, Y. Zhou, W. Zhang and C. Lu, *RSC Adv.*, 2016, **6**, 67556–67564.
- 31 N. Sutradhar, A. K. Biswas, S. K. Pahari, B. Ganguly and A. B. Panda, *Chem. Commun.*, 2014, **50**, 11529–11532.
- 32 P. Mikrut, D. Mitoraj, R. Beranek and W. Macyk, *Appl. Surf. Sci.*, 2021, **566**, 150662.
- 33 D. Sun, W. Yang, L. Zhou, W. Sun, Q. Li and J. K. Shang, *Appl. Catal., B*, 2016, **182**, 85–93.
- 34 H. Zhou, M. Wang, F. Kong, Z. Chen, Z. Dou and F. Wang, *J. Am. Chem. Soc.*, 2022, **144**, 21224–21231.
- 35 H. Wu, L. Zhang, A. Du, R. Irani, R. van de Krol, F. F. Abdi and Y. H. Ng, *Nat. Commun.*, 2022, **13**, 6231.
- 36 H. Wu, R. Irani, K. Zhang, L. Jing, H. Dai, H. Y. Chung, F. F. Abdi and Y. H. Ng, *ACS Energy Lett.*, 2021, **6**, 3400–3407.
- 37 M.-S. Kim, S.-H. Chung, C.-J. Yoo, M. S. Lee, I.-H. Cho, D.-W. Lee and K.-Y. Lee, *Appl. Catal., B*, 2013, **142–143**, 354–361.
- 38 J. Li, M. Li, X. Yang, S. Wang, Y. Zhang, F. Liu and X. Liu, *ACS Appl. Mater. Interfaces*, 2019, **11**, 33859–33867.
- 39 Y. Xu, K. Shi, T. Ren, H. Yu, K. Deng, X. Wang, Z. Wang, H. Wang and L. Wang, *Small*, 2022, **18**, 2203335.
- 40 P. Mikrut, M. Kobielski and W. Macyk, *Electrochim. Acta*, 2019, **310**, 256–265.
- 41 W. P. Utomo, H. Wu and Y. H. Ng, *Small*, 2022, **18**, 2200996.
- 42 X. Zhang, L. Luo, R. Yun, M. Pu, B. Zhang and X. Xiang, *ACS Sustainable Chem. Eng.*, 2019, **7**, 13856–13864.
- 43 Y. Zhang, J. Hu, C. Zhang, Y. Liu, M. Xu, Y. Xue, L. Liu and M. K. H. Leung, *J. Mater. Chem. A*, 2020, **8**, 9091–9098.
- 44 G. Liu, H. G. Yang, X. Wang, L. Cheng, H. Lu, L. Wang, G. Q. (Max) Lu and H.-M. Cheng, *J. Phys. Chem. C*, 2009, **113**, 21784–21788.
- 45 Y. Zhai, Y. Ji, G. Wang, Y. Zhu, H. Liu, Z. Zhong and F. Su, *RSC Adv.*, 2015, **5**, 73011–73019.
- 46 M. Fernández-Arias, M. Boutinguiza, J. del Val, A. Riveiro, D. Rodríguez, F. Arias-González, J. Gil and J. Pou, *Nanomaterials*, 2020, **10**, 300.
- 47 F. Yao, M. Jia, Q. Yang, F. Chen, Y. Zhong, S. Chen, L. He, Z. Pi, K. Hou, D. Wang and X. Li, *Water Res.*, 2021, **193**, 116881.
- 48 Z. Han, C. Choi, S. Hong, T.-S. Wu, Y.-L. Soo, Y. Jung, J. Qiu and Z. Sun, *Appl. Catal., B*, 2019, **257**, 117896.
- 49 H. Wang, L. Wang, D. Lin, X. Feng, Y. Niu, B. Zhang and F.-S. Xiao, *Nat. Catal.*, 2021, **4**, 418–424.
- 50 Z. Song, M. N. Banis, L. Zhang, B. Wang, L. Yang, D. Banham, Y. Zhao, J. Liang, M. Zheng, R. Li, S. Ye and X. Sun, *Nano Energy*, 2018, **53**, 716–725.
- 51 I. Jiménez-Morales, S. Cavaliere, D. Jones and J. Rozière, *Phys. Chem. Chem. Phys.*, 2018, **20**, 8765–8772.
- 52 L. Lin, S. Yao, R. Gao, X. Liang, Q. Yu, Y. Deng, J. Liu, M. Peng, Z. Jiang, S. Li, Y.-W. Li, X.-D. Wen, W. Zhou and D. Ma, *Nat. Nanotechnol.*, 2019, **14**, 354–361.
- 53 K. Zhu, F. Shi, X. Zhu and W. Yang, *Nano Energy*, 2020, **73**, 104761.
- 54 G. Wu, G. Zhao, J. Sun, X. Cao, Y. He, J. Feng and D. Li, *J. Catal.*, 2019, **377**, 271–282.
- 55 Y. Zhang, F. Du, R. Wang, X. Ling, X. Wang, Q. Shen, Y. Xiong, T. Li, Y. Zhou and Z. Zou, *J. Mater. Chem. A*, 2021, **9**, 17442–17450.
- 56 W. P. Utomo, H. Wu and Y. H. Ng, *Energies*, 2023, **16**, 27.
- 57 C. Wang, Y. Zhang, H. Luo, H. Zhang, W. Li, W. Zhang and J. Yang, *Small Methods*, 2022, **6**, 2200790.
- 58 O. Schmidt, A. Gambhir, I. Staffell, A. Hawkes, J. Nelson and S. Few, *Int. J. Hydrog. Energy*, 2017, **42**, 30470–30492.

- 59 C. A. Fernandez, N. M. Hortance, Y.-H. Liu, J. Lim, K. B. Hatzell and M. C. Hatzell, *J. Mater. Chem. A*, 2020, **8**, 15591–15606.
- 60 G.-F. Chen, Y. Yuan, H. Jiang, S.-Y. Ren, L.-X. Ding, L. Ma, T. Wu, J. Lu and H. Wang, *Nat. Energy*, 2020, **5**, 605–613.
- 61 D. Hartanto, G. Yuhaneke, W. P. Utomo, A. I. Rozafia, Y. Kusumawati, W. Dahani and A. Iryani, *RSC Adv.*, 2022, **12**, 5665–5676.
- 62 X. Wang, M. Zhu, G. Zeng, X. Liu, C. Fang and C. Li, *Nanoscale*, 2020, **12**, 9385–9391.
- 63 P. Wang, L. Yang, Y. Q. Gao and X. S. Zhao, *Nucleic Acids Res.*, 2015, **43**, 7207–7216.
- 64 X. Niu, X. Nie, C. Yang and J. G. Chen, *Catal. Sci. Technol.*, 2020, **10**, 1881–1888.
- 65 Y. Tang, C. Yang, M. Sheng, X. Yin and W. Que, *ACS Sustainable Chem. Eng.*, 2020, **8**, 12990–12998.
- 66 X. Teng, J. Wang, L. Ji, Y. Lv and Z. Chen, *Nanoscale*, 2018, **10**, 9276–9285.
- 67 C. Zhao, Y. Liang, W. Li, Y. Tian, X. Chen, D. Yin and Q. Zhang, *RSC Adv.*, 2017, **7**, 52614–52620.
- 68 K. Ao, Q. Wei and W. A. Daoud, *ACS Appl. Mater. Interfaces*, 2020, **12**, 33595–33602.
- 69 L. L. Zulfa, R. Ediati, A. R. P. Hidayat, R. Subagyo, N. Faaizatunnisa, Y. Kusumawati, D. Hartanto, N. Widiastuti, W. P. Utomo and M. Santoso, *RSC Adv.*, 2023, **13**, 3818–3834.
- 70 H. Wu, S. Qu, Z. Xie and Y. H. Ng, *ACS Appl. Energy Mater.*, 2022, **5**, 8419–8427.
- 71 G. Yuhaneke, A. I. Rozafia, W. P. Utomo, A. Iryani and D. Hartanto, *Malays. J. Fundam. Appl. Sci.*, 2022, **18**, 463–472.
- 72 H. Y. Chung, R. J. Wong, R. Amal and Y. H. Ng, *Energy Fuels*, 2022, **36**, 11550–11558.
- 73 X. Fu, X. Zhao, X. Hu, K. He, Y. Yu, T. Li, Q. Tu, X. Qian, Q. Yue, M. R. Wasielewski and Y. Kang, *Appl. Mater. Today*, 2020, **19**, 100620.
- 74 E. Pérez-Gallent, M. C. Figueiredo, I. Katsounaros and M. T. M. Koper, *Electrochim. Acta*, 2017, **227**, 77–84.
- 75 S.-E. Bae and A. A. Gewirth, *Faraday Discuss.*, 2008, **140**, 113–123.